Nano Research

Open Access

Research Article

Large-area bow-tie nanoantenna array for high-power high-order harmonic generation by field enhancement of surface plasmon resonance

Yong Soo Kim[1,4,§], Yeongkon Jeong[1,2,§], Young Jun An[1,2], Young Woo Jeong[3], Ju Han Lee[4] ✉, and Young Min Jhon[1] ✉

[1] *Sensor System Research Center, Korea Institute of Science and Technology (KIST), Seoul 02792, Republic of Korea*
[2] *School of Electrical Engineering, Korea University, Seoul 02841, Republic of Korea*
[3] *Advanced Analysis and Data Center, Korea Institute of Science and Technology (KIST), Seoul 02792, Republic of Korea*
[4] *School of Electrical and Computer Engineering (Brain Korea 21 Four), University of Seoul, Seoul 02504, Republic of Korea*
[§] *Yong Soo Kim and Yeongkon Jeong contributed equally to this work.*

Cite this article: *Nano Research*, **2025**, *18*, 94907040. https://doi.org/10.26599/NR.2025.94907040

ABSTRACT: A bow-tie nanoantenna (BNA) array is one of the nanostructures most suitable for maximizing the field enhancement effect by surface plasmon resonance (SPR). Among several applications, the BNA array can enhance the intensity of pump lasers, especially in high-order harmonic generation (HHG). In this study, the focused ion beam (FIB)-scanning electron microscopy AutoScript 4 toolkit was used to automate the entire process of FIB milling and reduce the time required, spending less than 3 h fabricating a large area of 50 μm × 50 μm, and at the same time improving the quality of the BNA array through internal object control. In addition, diamond, which has a thermal conductivity more than 90 times higher than sapphire, was used as a substrate for the BNA array. For the first time in the world, the BNA was not damaged even when exposed to a laser intensity of 10^{12} W/cm^2 for a long time. Surface-enhanced Raman scattering (SERS) measurements were performed by combining 4-aminothiophenol (4-ATP) as a probe molecule in fabricated large-area BNA arrays, confirming the large electric field enhancement in the gap of BNA, and the calculated enhancement factor (EF) was 8.83 × 10^9. In addition, the electric field simulation and heat transfer simulation using the finite element method (FEM) showed a 250-fold increase in the electric field based on the input unit electric field (1 V/m), a 9 times faster heat diffusion rate for the diamond substrate than the sapphire substrate based on the fall time, and 67.5 times faster the heat diffusion rate for the diamond substrate than the sapphire substrate based on the stabilization time. Therefore, both the experimental and simulation results showed that the fabricated large-area BNA array can be applied to high-power HHG.

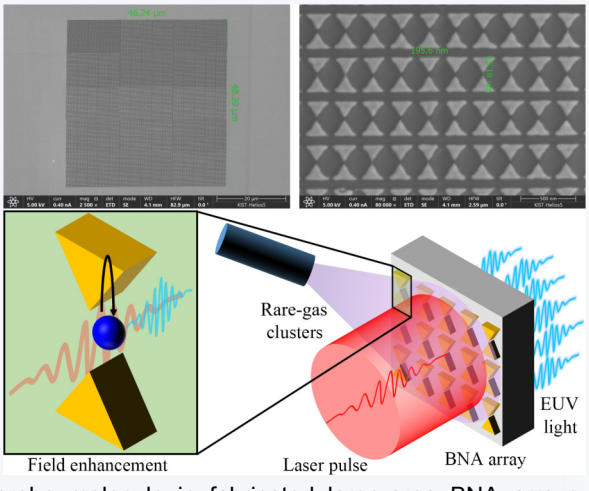

KEYWORDS: bow-tie nanoantenna, surface plasmon resonance, field enhancement, surface-enhanced Raman scattering, high thermal conductivity, high laser intensity

1 Introduction

In the late 1960s, full-scale research on surface plasmon resonance (SPR) began approximately 50 years after the first discovery of the surface plasmon phenomenon called Wood's anomaly [1, 2] in the early 1900s, starting with the optical excitation of surface plasmons through attenuated total reflection by Kretschmann and Raether [3], and Otto [4]. Later discussions on the use of SPR as a sensor began in the 1980s, and extensive research on SPR as a chemical and biosensors began in the 1990s [5–10], and the concept of a nanoantenna was introduced from the surface plasma phenomenon of metal nanoparticles for the first time in 1985 [11]. With the introduction of this concept, the discovery of surface-enhanced Raman scattering (SERS) [12–14] promoted many

Received: July 26, 2024; **Revised:** September 10, 2024
Accepted: September 18, 2024

✉Address correspondence to Ju Han Lee, j.h.lee@ieee.org; Young Min Jhon, ymjhon@kist.re.kr

theoretical studies to predict the enhancement of electromagnetic fields near metal nanoparticles and nanoclusters in the 1980s [15–17]. Over the next 30 years, considerable research and development in a new field called nanoplasmonics were established. In the 2000s, there have been impressive developments in ultra-fine nanostructures, such as achieving nanogap plasmon antennas of less than 20 nm with the development of ultra-fine process manufacturing technologies, such as E-beam lithography [18–22] and focused ion beam (FIB) milling [23–29]. In particular, a nanoantenna called a bow-tie has been studied for the effects of various parameters, such as nanostructure design [30, 31] and fabrication [32, 33], size or length [30, 34], gap [27, 28, 35, 36], and asymmetry [37, 38], due to the strong electric field enhancement in the nanogaps between pointed tips. The formation of strong SPR fields between nanogaps can be utilized for the detection of single molecules or larger proteins [39], and it has also been shown that they can be used for the ablation of cell tissues due to the potential thermal effect of BNAs exhibiting highly restricted plasmonic resonance fields [40, 41].

E-beam lithography was used widely in the early research on bow-tie nanoantennas (BNAs), but it was difficult to achieve a gap of less than 10 nm because of the resolution limit. A special resist called negative-tone hydrogen silsesquioxane (HSQ) must be used to achieve a gap below 10 nm with E-beam lithography [18, 19, 22, 42]. The technical difficulty of removing the resist within a short time is required because the development time is short, and the space between the BNA is considerably larger than the bow-tie gap. Therefore, FIB milling [23–29] is used mainly as a manufacturing method for BNAs with a gap below 10 nm, but the processing time is very long, so it is unsuitable for manufacturing large-area BNA arrays. Most BNA arrays fabricated in previous studies have an area of less than 20 μm × 20 μm [23–26]. This area issue can directly affect the harmonic yield of high-order harmonic generation (HHG) using a BNA array. The spot size of the laser beam at the location where the harmonics are generated is more than several tens of μm larger than the conventional BNA array. Previous studies showed that the size of the rare-gas cluster in HHG can affect the higher photon yield [43–46], suggesting that the larger the size of the BNA array that can capture clusters, the higher the energy of harmonics. In addition, BNA arrays in HHG must withstand the very high intensity of the laser beam. Since Kim's study [23], several studies [24–26] on BNA arrays for HHG have been published, and no BNA arrays that can withstand an intensity of 10^{12} W/cm^2 or more for a long time have been published. It is necessary to examine the substrate as a way to increase the thermal durability of BNA that can withstand high intensity, but most studies were only interested in metals, the material of BNA, and a change in the material of the BNA substrate was not mentioned except for mica mentioned in Sivis's study [25]. The present study proposed diamond, which has a much higher thermal conductivity than sapphire or mica, as a substrate for the BNA array for HHG, and predicted that thermal durability could increase by calculating the heat diffusion time through finite element method (FEM) simulation. Subsequently, a laser-induced damage threshold (LIDT) test showed one order of magnitude (10^{12} W/cm^2) higher thermal durability than the existing sapphire substrate BNA array. Using AutoScript 4, a FIB- scanning electron microscopy (SEM) toolkit, the entire process of FIB milling (loading milling patterns, auto-eucentric, and moving a high-precision stage) is automated by Python coding, drastically shortening the long processing time, which is the weakness of FIB milling. Hence, this study fabricated large-area BNA arrays of 50 μm × 50 μm, which are comparable to the beam spot size of the pump laser for HHG. The fabricated large-area BNA arrays showed that the effect of electric field enhancement by SPR sufficiently occurs through SERS measurements and calculations of the enhancement factors and thus show potential for high-power HHG because of the application of higher laser intensity and the larger area that can cause interactions with the rare-gas clusters.

2 Experimental

2.1 Preparation of nanoantenna array

BNA arrays were initially fabricated using E-beam lithography, but the manufacturing method was changed to FIB milling due to resolution limitations (Fig. S1(a) in the Electronic Supplementary Material (ESM)). Therefore, bow-tie gold nanoantenna arrays were fabricated on gold films deposited on a single crystal chemical vapor deposition (CVD) diamond substrate using the FIB milling techniques, as shown in Fig. 1. Here, an adhesion layer was placed on the substrate before depositing the gold film, and titanium or chromium was used as the adhesive material (Fig. 1(a)). Various deposition processes can produce gold films on thin adhesives, and the 30 nm thick gold films were deposited using an electron beam evaporator (EI-5K, ULVAC), as shown in Fig. 1(b). In the next process, a focused Ga^+ ion beam (Helios G5 HX, Thermo Fisher Scientific) was scanned over the substrate, and unnecessary gold thin films were removed by ion collisions (Fig. 1(c)), leaving the desired gold nanoantenna structure at the target location (Fig. 1(d)). Software called AutoScript 4 (Thermo Fisher Scientific) was used for the FIB process. The processing time can be shortened significantly by automating the entire process by loading milling patterns, auto eucentric function, and moving high-precision stage based on five-axis piezo motors, so the fabrication of large-area BNA arrays was enabled, as shown in Fig. 2(c). The time it took to fabricate a 50 μm × 50 μm BNA array on a gold film-deposited substrate, as shown in Fig. 2(c), was less than three hours. In addition, a typical FIB SEM system loaded a bitmap file to proceed with the process, but AutoScript 4 drawed the desired pattern through Python coding. This pattern consisted of small circles as internal objects, and the size and number can be adjusted, so the quality of FIB milling was better than the BMP method. The size and spacing of internal objects were optimized to 94.8 pm and 6.25 nm, respectively, and the total number of objects was 131,040 (see Fig. S2(d) in the ESM). Figure 2(a) shows the FIB milling pattern loaded through AutoScript 4 with the optimized size and spacing. In the FIB-SEM system, 64 × 20 BNAs can be formed within the field of view (FOV) of the ion beam. Figure 2(b) presents the patterning results. The size was 15.30 μm × 9.56 μm when patterning was done once within the FOV, and this was repeated 15 times (3 × 5) to produce a large-area nanoantenna array of up to 50 μm × 50 μm, as shown in Fig. 2(c). The nanoantenna size and gap satisfied 200 and 20 nm, respectively (Fig. 2(d)). In addition, since the consistent quality of the gap size of the nanoantenna highly affected the performance of the fabricated BNA arrays, a statistical analysis was performed on the deviation of the nanogap size. The data measured from 10 different random nanoantennas in 15 patterning areas were collected (150 in total), and the mean and

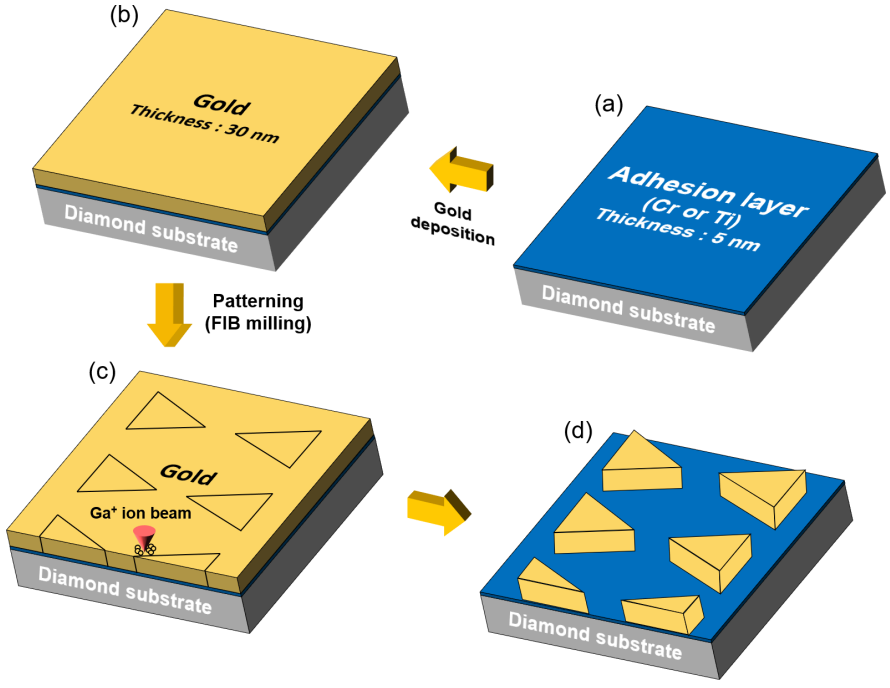

Figure 1 Fabrication process of BNA arrays: (a) To improve mechanical stability so that diamond and gold adhere well, an adhesive layer, such as chromium or titanium, was coated on the substrate to a thickness of 5 nm. (b) A 30 nm thick gold film was deposited on the substrate. (c) FIB milling process: Remove the area outside the bow-tie pattern with a gallium ion beam. (d) Only the BNAs remain on the substrate to complete the array.

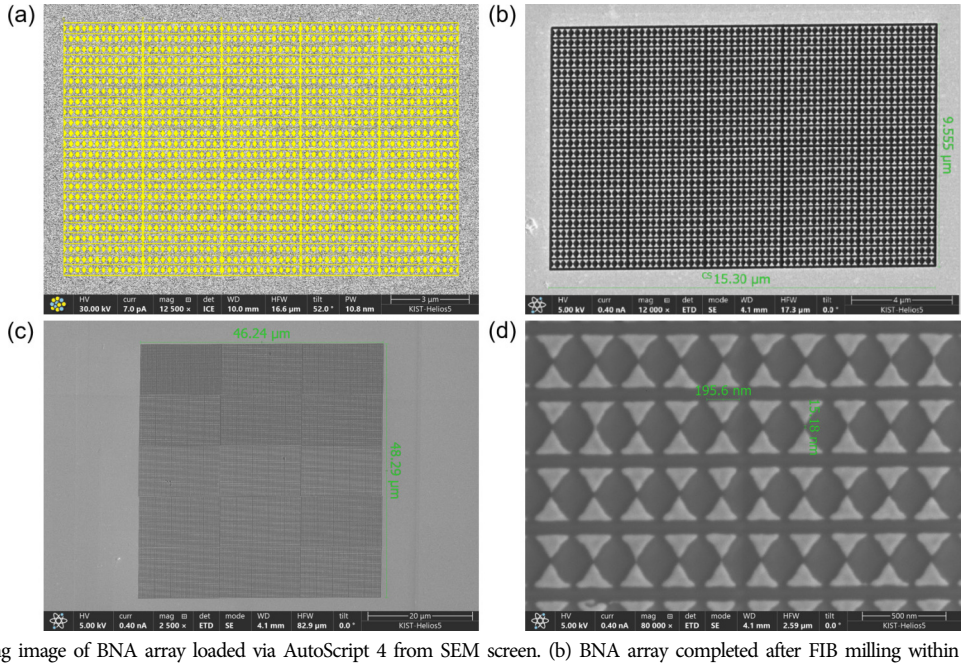

Figure 2 (a) Patterning image of BNA array loaded via AutoScript 4 from SEM screen. (b) BNA array completed after FIB milling within the FOV. The size was measured to be 15.30 µm in width and 9.555 µm in height, respectively. (c) After moving the sample stage, FIB milling was performed 15 times (3 × 5) at the next location to complete the final BNA array. The measured size was 46.24 µm in width and 48.29 µm in height, respectively. (d) Measurements on the bow-tie nanoantenna inside the fabricated BNA array. When one was measured at random, the width was measured to be 195.6 nm, and the gap was measured to be 15.18 nm.

relative standard deviation (RSD) were calculated to be 14.90 nm and 10.72%, respectively (see Fig. S3 in the ESM).

2.2 Laser-induced damage threshold test

The optical system and sample were installed in the chamber to test thermal damage caused by a laser beam, as shown in Fig. 3. The experiment was conducted with the chamber maintained in a vacuum because laser intensity above 10^{12} W/cm^2 generated air plasma in the atmosphere and destroyed the shape of the beam. A Ti:sapphire femtosecond laser system (Spitfire Ace, Spectra-Physics) was used as the laser source, with a central wavelength, repetition rate, pulse width, and pulse energy of 796 nm, 1 kHz, 35 fs, and 5 mJ, respectively. A concave mirror (CM) with a focal length of 1 m was placed to focus the laser beam, and a beam splitter (BS) of 10:90 (R:T) and 50:50 (R:T) was placed appropriately for each experiment to control the laser intensity. The laser pulse was

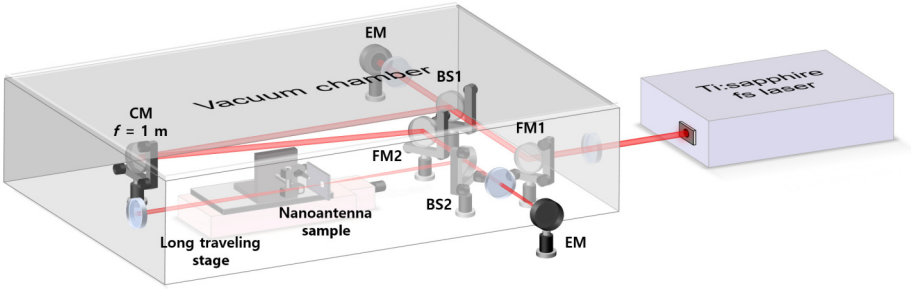

Figure 3 Schematic of the LIDT test setup. A Ti:sapphire laser with a central wavelength of 800 nm, pulse width of 35 fs, average energy of 5 mJ, and repetition rate of 1 kHz was used, and the test was conducted in a vacuum chamber because of the high laser intensity. The laser beam was focused on the BNA sample using a flat mirror (FM), BS, CM, and 150 mm long travel motorized stage. The energy of the laser pulse can be measured using an EM in the transmission path of each beam splitter.

linearly polarized horizontally and was P-polarized for each optical system. The reflectance of the two beam splitters for P-polarized light was calculated to be 3.59% and 34%, respectively (see Fig. S4 in the ESM). An energy meter (EM) was placed on the transmission path of the beam splitters to monitor the energy of the laser pulse in real-time, and the nanoantenna sample can be moved to the desired location through a 150 mm long travel stage.

2.3 Raman spectroscopy

The SERS of the BNA arrays was evaluated by introducing 4-aminothiophenol (4-ATP; Sigma–Aldrich) as probe molecules. The 4-ATP was diluted in ethanol, and a 20-μL droplet of 4-ATP solution (5.0×10^{-3} M) was dropped on the nanoantenna substrate and dried at room temperature. The Raman spectra were measured with an inVia Reflex Raman microscopy (Renishaw). The samples were excited by a second harmonic 532 nm beam of a Nd:YAG laser through a ×100 (NA = 0.75) objective lens. The power and diameter of the laser beam were 5 mW and 1 μm, respectively.

2.4 Simulation of BNA array

The electric field intensity, distribution, and heat transfer for BNA arrays were analyzed using full-wave electromagnetic simulations based on the FEM, a numerical analysis method. The simulations were performed using COMSOL multiphysics, a commercial FEM solver. The dielectric coefficient, thermal conductivity, and other parameters of gold, diamond, and sapphire were obtained from Johnson and Christy [47], Phillip and Taft [48], and Malitson and Dodge [49], respectively. More details on modeling and calculations were available in Section S7 in the ESM.

3 Results and discussion

Figure 4 presents a schematic diagram of the BNA, the optimization parameters of the BNA array simulation, and the results. Various geometric parameters, such as gap, angle, width, and height, affect the electric field enhancement by SPR of nanoantennas, as shown in Fig. S6(a) in the ESM. The parameters were optimized to set the resonance frequency to 800 nm because an 800 nm Ti:sapphire laser is used as a pump laser source for HHG, as shown in Fig. 4(a). The width, length, gap size, and period of the gold BNA were 200, 200, 10, and 65 nm, respectively, and the thickness and angle were 30 nm and 53.13°, respectively. Figures 4(b) and 4(c) present the s-parameter and electric field

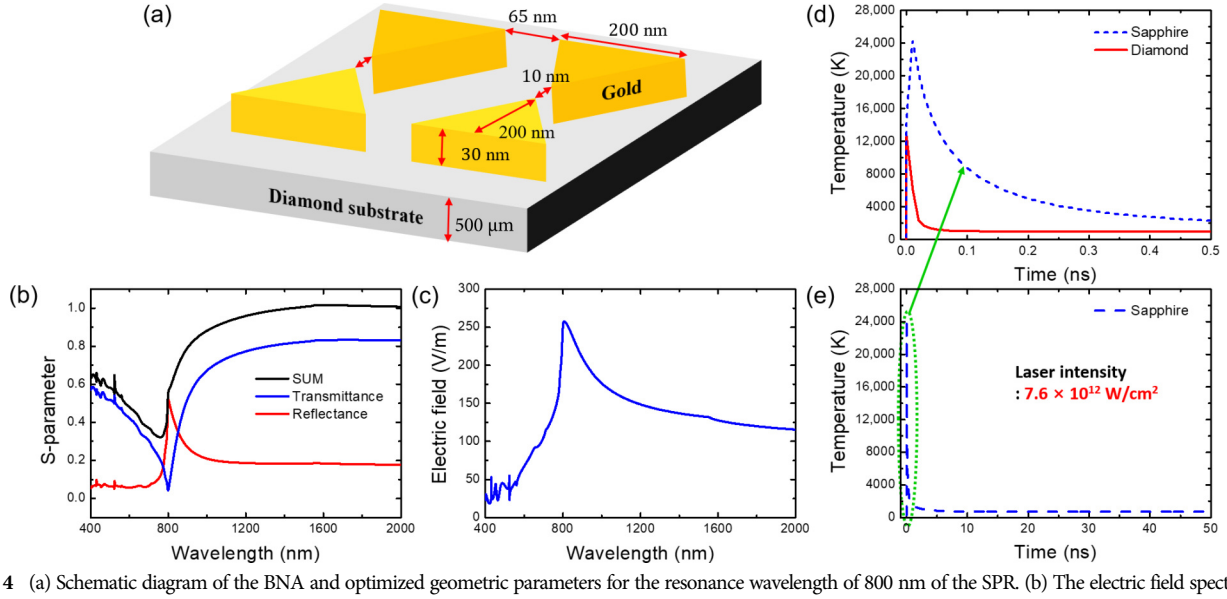

Figure 4 (a) Schematic diagram of the BNA and optimized geometric parameters for the resonance wavelength of 800 nm of the SPR. (b) The electric field spectrum in the VIS–IR wavelength range was enhanced by the field enhancement effect of the BNA. The input electric field was 1 V/m, enhanced 250 times at 800 nm. (c) The s-parameter spectrum was calculated when light was incident perpendicularly from the upward direction on the BNA. Absorption and reflectance were highest at 800 nm due to SPR. (d) Temperature graphs were calculated for sapphire and diamond substrates when a laser intensity of 12 orders of magnitude was incident. Sapphire has a higher temperature peak and a very slow heat diffusion rate than diamond. (e) Temperature graph was calculated for a sapphire substrate when a laser intensity of 12 orders of magnitude was incident. The range of *x*-axis was set to 50 ns to show the time taken for temperature stabilization.

enhancement spectra in the visible–infrared (VIS–IR) wavelength band, respectively. The resonance frequency was 800 nm because absorption due to the SPR phenomenon occurs at 800 nm (Fig. 4(b)). The field enhancement of up to 250 times was possible at 800 nm when the input electric field was 1 m/W (Fig. 4(c)). These two results support that the previously selected geometric parameters were optimized for the resonance frequency of 800 nm. In addition, high-order harmonics can be generated even with relatively low laser intensity owing to the increasing laser intensity by more than two orders through this field enhancement, and several research results have proven experimentally that this is possible [23–26].

The parameters for heat diffusion include the thermal conductivity of the substrate, the width and length of the nanoantenna, and the types of top layer and bottom layer, as shown in Fig. S7(a) in the ESM. The width and length of the nanoantenna are the same as the values of electric field enhancement simulation, and the substrate material and nanoantenna material are diamond and gold, respectively. Figure 4(d) shows the simulation results for heat transfer analysis of the BNA array using the diamond substrate. Other studies have used sapphire (Al_2O_3) as a substrate material. On the other hand, considering the BNA array exposed to high intensity [23–26], it was estimated that diamond, which has much higher thermal conductivity than sapphire, will withstand thermal damage at higher laser intensity than when sapphire is used.

At room temperature (300 K), the thermal conductivities of diamond and sapphire are 2200 and 24 W/(m·K), respectively [50, 51]. Therefore, the calculation was performed by setting diamond as the substrate material, and based on the laser intensity of 7.6×10^{12} W/cm^2, the peak temperature was calculated to be 12,641 and 24,287 K for diamond and sapphire, respectively, as shown in Fig. 4(e). To compare with the diamond substrate, the simulation results for the sapphire substrate were also plotted. To show the time required for temperature stabilization when the sapphire substrate was used, the *x*-axis range was set to 50 ns, as shown in Fig. 4(d). Based on the time it takes for the temperature to drop and stabilize, the heat diffusion time was calculated to be 67.5 times faster when using a diamond substrate (0.24 ns) than a sapphire substrate (16.2 ns). In addition, based on the fall time (90% to 10% of the peak value), the calculated heat diffusion time was nine times faster when using a diamond substrate (0.05 ns) compared to a sapphire substrate (0.45 ns).

BNA arrays fabricated for HHG require high thermal durability. According to the research results of other groups published in the past, an intensity of at least 10^{13} W/cm^2 is required to generate high-order harmonics. Therefore, a laser intensity of 10^{11} W/cm^2 was generally incident on the nanoantenna, and an intensity of 10^{13} W/cm^2 was enabled by the electric field enhancement effect [23–26]. On the other hand, intensities above 12 orders are difficult to apply because the gold is damaged because of the thermal damage caused by the laser beam. Only Pfullmann's study reported that it was possible to apply an intensity of 1.3×10^{12} W/cm^2, but it was reported that some nanoantennas were damaged [26]. A recent study on gold processing using a femtosecond laser with a wavelength of 800 nm reported that the energy threshold for thermal damage to gold was 0.19 J/cm^2 [52]. If converted to intensity, the pulse width is 35 fs, so the intensity is approximately 5.4×10^{12} W/cm^2. Moreover, if heat is released quickly structurally, this suggests that an intensity of 12 orders or more can be applied sufficiently to BNA arrays. The possibility was verified by performing a LIDT test with an irradiating laser intensity of 12–13 orders to the BNA arrays.

Figures 5(a), 5(c), 5(e), and 5(g) are SEM images of BNA arrays before irradiation with a laser beam, and Figs. 5(b), 5(d), 5(f), and 5(h) are SEM images of BNA arrays after irradiation. For convenience, the BNA array in Figs. 5(a), 5(c), 5(e), and 5(g) is called array #1, and the BNA array in Figs. 5(b), 5(d), 5(f), and 5(h) is called array #2. Arrays #1 and #2 are samples fabricated under same process conditions, and the order of magnitude for the laser intensity was the same but the coefficient was set differently to check how much each sample can withstand thermal damage caused by the laser pulse. The two arrays were irradiated with laser beams at intensities of 5.8×10^{13} and 2.6×10^{13} W/cm^2, respectively (see Section S4 in the ESM for calculations of laser intensity). In array #1, which was exposed to very high intensity, most of the gold film was damaged and the bow-ties fell off or lost their shape and stuck in a row. Array #2, whose intensity is one order lower than that of array #1, has many bow-ties that maintain their shape, but the damage was too severe for the SPR effect to occur normally.

Figures 6(a) and 6(c) are SEM images of the BNA array before irradiation with a laser beam, and Figs. 6(b) and 6(d) are SEM images of the BNA array after irradiation. The BNA array is a sample fabricated under the same process conditions as the samples in Fig. 5, and test was performed with the laser intensity lowered by one order of magnitude from the condition in Fig. 5 to confirm thermal damage caused by the laser. A BNA array was irradiated with a laser beam with an intensity of 7.4×10^{12} W/cm^2. The exposure time was 30 min. Unlike the two arrays in Fig. 5, all BNAs remained intact and without damage. These experimental results fit well with the tendency of the heat diffusion simulation results in Fig. 4(d) and are the world's first undamaged BNA array with a laser intensity of 12 orders.

The BNA arrays for HHG must be proven to have high thermal durability and ensure that the SPR phenomenon occurs appropriately. SERS is commonly used to confirm SPR in various nanostructures, including nanogaps, nanoparticles, and nanoantennas. Therefore, SERS measurements were taken to demonstrate the SPR of the large-area BNA array. Probe molecules used in SERS include rhodamine 6G (R6G) [53, 54], 4-ATP [55–59], and 4-mercaptopyridine (4-MPy) [35], and 4-ATP was chosen because it is used widely in gold or silver nanostructures and is inexpensive. Figure 7(a) is the spectrum measured for comparison with SERS as the normal Raman spectrum of bulk 4-ATP. The basic Raman peaks of 4-ATP showed peaks at 470, 1090, and 1595 cm^{-1}. Figure 7(b) is the SERS spectrum measured after absorbing 5×10^{-3} M 4-ATP solution into a BNA array on a diamond substrate. A very large peak occurred at 1330 cm^{-1}, so the SERS signal peaks of 4-ATP are not easily visible. The peak at 1330 cm^{-1} is a diamond peak because of the diamond substrate [60]. The laser beam can be transmitted, and the Raman peak of the diamond can be measured because the diamond substrate is exposed directly in the area where the gold film outside the bow-ties is removed by FIB milling, or the gold film thickness of the BNA is 30 nm, which is thinner than the penetration depth of the gold at 532 nm [61, 62]. Figure 7(c) presents a spectrum in which the diamond peak at 1330 cm^{-1} was removed from the SERS spectrum in Fig. 7(b). In SERS measurements, detection reproducibility is an important indicator for evaluating the performance of the BNA array, so the reproducibility evaluation for SERS was performed. The spectra measured 10 times at different locations in a 50 μm × 50 μm area of the BNA array were collected, and statistical analysis was performed. The average and RSD of the three characteristic

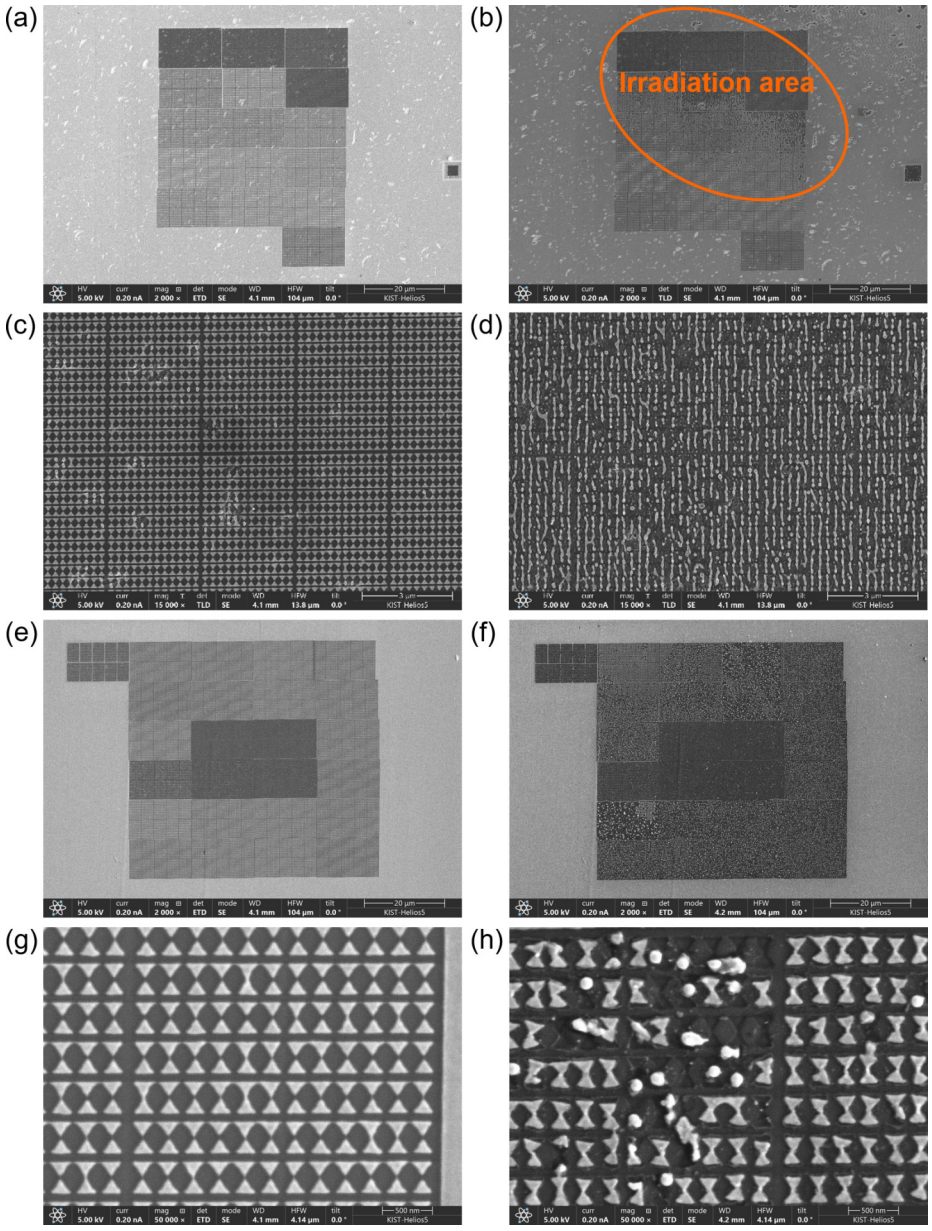

Figure 5 (a), (c), (e), and (g) Before irradiating with a laser beam. (b), (d), (f), and (h) After irradiating with a laser beam. (a)–(d) and (e)–(h) are the same BNA array, respectively. For convenience, the BNA array in (a)–(d) is referred to as array #1, and the BNA array in (e)–(h) is referred to as array #2. Arrays #1 and #2 are samples fabricated under the same process conditions, and the order of the laser intensity was the same but the coefficient was set differently to confirm thermal damage caused by the laser. Array #1 was irradiated with a laser intensity of 5.8×10^{13} W/cm^2, and array #2 was irradiated with a laser intensity of 2.6×10^{13} W/cm^2. In both arrays, the gold film was damaged by exceeding the LIDT.

peaks of 4-ATP (470, 1090, and 1595 cm^{-1}) were calculated to be 10.20%, 5.82%, and 7.89%, respectively (see Fig. S5 in the ESM). In the SERS spectrum of 4-ATP, the peak in the 1590 cm^{-1} band, which is used as the reference peak, was measured as the strongest signal [12–16]. The signal was normalized and compared based on 1090 cm^{-1}, which is the strongest in bulk 4-ATP, to check how much the SERS signal has been enhanced compared to the normal Raman spectrum. Figure 7(d) shows the spectra compared by normalizing the spectrum of bulk 4-ATP and the SERS spectrum of 4-ATP enhanced by the BNA array based on 1090 cm^{-1}. The magnitude of the peak at 1595 cm^{-1} compared to normal Raman was 4.7 times larger. Calculating with reference to the parameters in Table S1 in the ESM, the enhancement factor (EF) was calculated to be 8.83×10^9 (see Section S6 in the ESM), which is larger than that of other groups [11–13, 15]. Therefore, the SPR effect occurs sufficiently and properly in the BNA arrays produced in this study.

4 Conclusions

The FIB milling process was automated through the AutoScript 4 toolkit based on Python coding and reduced the processing time to fabricate BNA arrays for HHG. The fabricated BNA arrays had a large area of 50 μm × 50 μm, which corresponds to the beam spot size of the pump laser for generating higher-order harmonics, so it expands the area that can react with the rare-gas clusters. In addition, diamond with a thermal conductivity more than 90 times higher than sapphire was selected as the substrate to improve the thermal durability of the BNA arrays, followed by FEM simulations

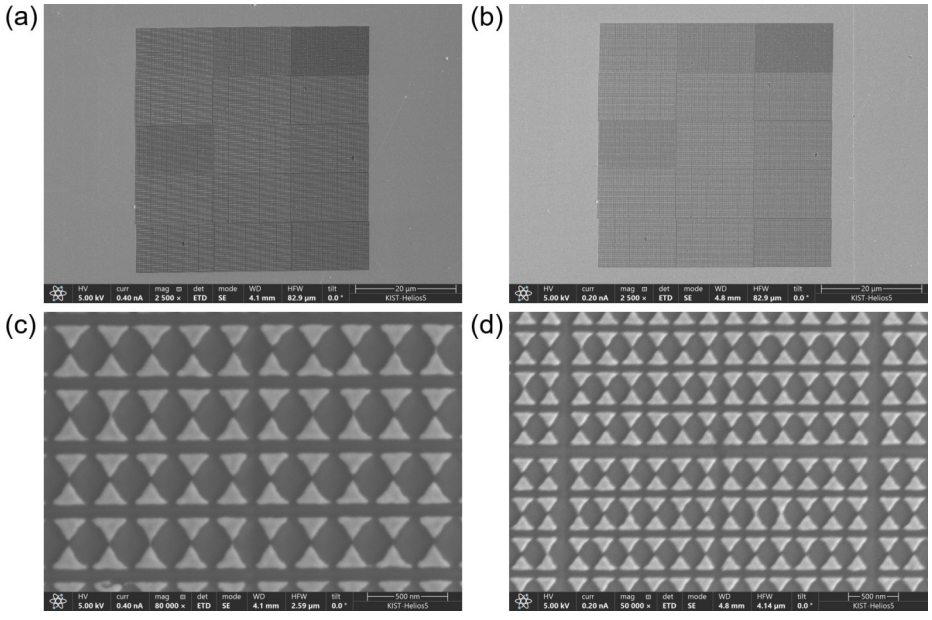

Figure 6 (a) and (c) Before irradiating with a laser beam. (b) and (d) After irradiating with a laser beam. The BNA array is a sample fabricated under the same process conditions as the samples in Fig. 5, and test was performed with the laser intensity lowered by one order of magnitude from the condition in Fig. 5 to confirm thermal damage caused by the laser. The BNA array was irradiated with a laser intensity of 7.4×10^{12} W/cm^2. All BNAs maintain bow-tie shapes without damage.

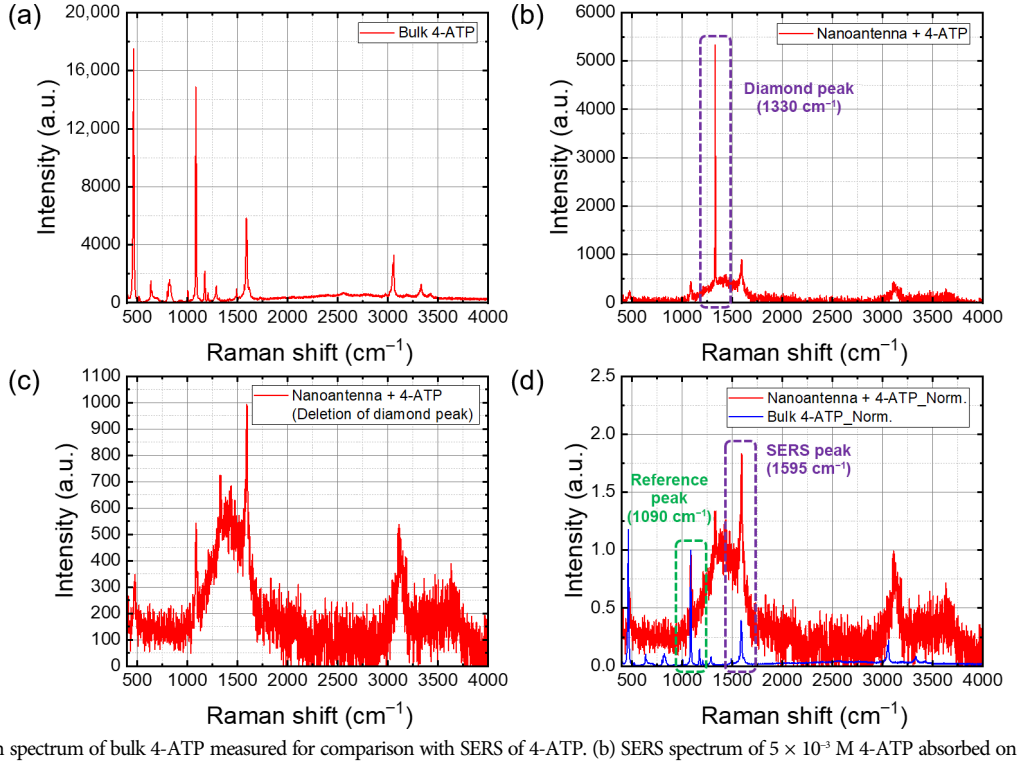

Figure 7 (a) Raman spectrum of bulk 4-ATP measured for comparison with SERS of 4-ATP. (b) SERS spectrum of 5×10^{-3} M 4-ATP absorbed on the fabricated BNA array. (c) SERS spectrum of 5×10^{-3} M 4-ATP after eliminating 1330 cm^{-1} peak of diamond film. (d) Comparison of the SERS peak (1595 cm^{-1}) in the bulk 4-ATP spectrum and the SERS spectrum of 5×10^{-3} M 4-ATP after normalization based on the reference peak (1090 cm^{-1}) of 4-ATP.

under the same conditions as the large-area BNA array to calculate the electric field enhancement and heat diffusion, and the LIDT test and SERS measurements showed good agreement with the simulation results. As a result of the electric field enhancement simulation, the electric field increased 250-fold based on the input of the unit electric field (1 V/m). As a result of the heat transfer simulation, the BNA array of the diamond substrate decreased nine times faster based on the fall time and 67.5 times faster based on the stabilization time, and the peak temperature was half the level of the sapphire. In the LIDT test, there was no damage to the BNA array even when exposed to an intensity of 7.6×10^{12} W/cm^2 for a long time. After the SERS measurements, the characteristic peak at 1595 cm^{-1} in SERS was increased 4.65-fold compared to normal Raman spectrum, and the EF calculation result was 8.83×10^9. In

this way, the simulation and experimental results showed that the fabricated large-area BNA arrays were suitable for the nanostructures for high-power HHG by field enhancement of SPR and that high-power HHG is feasible. Future studies will perform high-power HHG experiments with large-area BNA arrays fabricated using the HHG source reported elsewhere [63].

Electronic Supplementary Material: Supplementary material (the description of comparison of E-beam lithography and FIB milling in nanoantennas, characterization of BNA arrays using AutoScrip4 of FIB-SEM, deviation of the gap size of the fabricated nanoantenna arrays, calculations of laser intensity in LIDT test, evaluation of reproducibility of SERS measurements, and calculation of EF, and FEM simulations) is available in the online version of this article at https://doi.org/10.26599/NR.2025.94907040.

Data availability

All data needed to support the conclusions in the paper are presented in the manuscript and the Electronic Supplementary Material. Additional data related to this paper may be requested from the corresponding author upon request.

Acknowledgements

This work was supported by the Korea Institute of Science and Technology Institutional Program (2E33162) and the National Research Foundation of Korea (NRF) grant funded by the Korea government (MSIT) (No. NRF-2021R1A5A1032937).

Declaration of competing interest

All the contributing authors report no conflict of interest in this work.

Author contribution statement

Y. S. K.: Writing – original draft, experimental design, formal analysis, data curation. Y. J.: Conceptualization, investigation, software, data curation. Y. J. A.: Software, data curation. Y. W. J.: Investigation, resources. J. H. L.: Project administration, validation, writing-Review and Editing. Y. M. J.: Project administration, validation, writing – review & editing, funding acquisition. All the authors have approved the final manuscript.

Use of AI statement

None.

References

[1] Wood, R. W. On a remarkable case of uneven distribution of light in a diffraction grating spectrum. *Proc. Phys. Soc. London* **1902**, *18*, 269–275.

[2] Wood, R. W. XXVII. Diffraction gratings with controlled groove form and abnormal distribution of intensity. *Lond. Edinburgh Dublin Philos. Mag. J. Sci.* **1912**, *23*, 310–317.

[3] Kretschmann, E.; Raether, H. Notizen: Radiative decay of non radiative surface plasmons excited by light. *Z. Naturforsch. A* **1968**, *23A*, 2135–2136.

[4] Otto, A. Excitation of nonradiative surface plasma waves in silver by the method of frustrated total reflection. *Z. Phys. A Hadrons Nucl.* **1968**, *216*, 398–410.

[5] Stenberg, E.; Persson, B.; Roos, H.; Urbaniczky, C. Quantitative determination of surface concentration of protein with surface plasmon resonance using radiolabeled proteins. *J. Colloid Interface Sci.* **1991**, *143*, 513–526.

[6] Löfås, S.; Malmqvist, M.; Rönnberg, I.; Stenberg, E.; Liedberg, B.; Lundström, I. Bioanalysis with surface plasmon resonance. *Sens. Actuators B Chem.* **1991**, *5*, 79–84.

[7] Liedberg, B.; Lundström, I.; Stenberg, E. Principles of biosensing with an extended coupling matrix and surface plasmon resonance. *Sens. Actuators B Chem.* **1993**, *11*, 63–72.

[8] Jorgenson, R. C.; Yee, S. S. A fiber-optic chemical sensor based on surface plasmon resonance. *Sens. Actuators B Chem.* **1993**, *12*, 213–220.

[9] Harris, R. D.; Wilkinson, J. S. Waveguide surface plasmon resonance sensors. *Sens. Actuators B Chem.* **1995**, *29*, 261–267.

[10] Lyon, L. A.; Musick, M. D.; Natan, M. J. Colloidal Au-enhanced surface plasmon resonance immunosensing. *Anal. Chem.* **1998**, *70*, 5177–5183.

[11] Wessel, J. Surface-enhanced optical microscopy. *J. Opt. Soc. Am. B* **1985**, *2*, 1538–1541.

[12] Fleischmann, M.; Hendra, P. J.; McQuillan, A. J. Raman spectra of pyridine adsorbed at a silver electrode. *Chem. Phys. Lett.* **1974**, *26*, 163–166.

[13] Jeanmaire, D. L.; van Duyne, R. P. Surface Raman spectroelectrochemistry: Part I. Heterocyclic, aromatic, and aliphatic amines adsorbed on the anodized silver electrode. *J. Electroanal. Chem. Interf. Electrochem.* **1977**, *84*, 1–20.

[14] Albrecht, M. G.; Creighton, J. A. Anomalously intense Raman spectra of pyridine at a silver electrode. *J. Am. Chem. Soc.* **1977**, *99*, 5215–5217.

[15] Gersten, J.; Nitzan, A. Electromagnetic theory of enhanced Raman scattering by molecules adsorbed on rough surfaces. *J. Chem. Phys.* **1980**, *73*, 3023–3037.

[16] Wokaun, A.; Gordon, J. P.; Liao, P. F. Radiation damping in surface-enhanced Raman scattering. *Phys. Rev. Lett.* **1982**, *48*, 957–960.

[17] Meier, M.; Wokaun, A.; Liao, P. F. Enhanced fields on rough surfaces: Dipolar interactions among particles of sizes exceeding the Rayleigh limit. *J. Opt. Soc. Am. B* **1985**, *2*, 931–949.

[18] Duan, H. G.; Hu, H. L.; Kumar, K.; Shen, Z. X.; Yang, J. K. W. Direct and reliable patterning of plasmonic nanostructures with sub-10-nm gaps. *ACS Nano* **2011**, *5*, 7593–7600.

[19] Duan, H. G.; Fernández-Domínguez, A. I.; Bosman, M.; Maier, S. A.; Yang, J. K. W. Nanoplasmonics: Classical down to the nanometer scale. *Nano Lett.* **2012**, *12*, 1683–1689.

[20] Schuck, P. J.; Fromm, D. P.; Sundaramurthy, A.; Kino, G. S.; Moerner, W. E. Improving the mismatch between light and nanoscale objects with gold bowtie nanoantennas. *Phys. Rev. Lett.* **2005**, *94*, 017402.

[21] Muskens, O. L.; Giannini, V.; Sánchez-Gil, J. A.; Rivas, J. G. Strong enhancement of the radiative decay rate of emitters by single plasmonic nanoantennas. *Nano Lett.* **2007**, *7*, 2871–2875.

[22] Koh, A. L.; Fernández-Domínguez, A. I.; McComb, D. W.; Maier, S. A.; Yang, J. K. W. High-resolution mapping of electron-beam-excited plasmon modes in lithographically defined gold nanostructures. *Nano Lett.* **2011**, *11*, 1323–1330.

[23] Kim, S.; Jin, J.; Kim, Y. J.; Park, I. Y.; Kim, Y.; Kim, S. W. High-harmonic generation by resonant plasmon field enhancement. *Nature* **2008**, *453*, 757–760.

[24] Sivis, M.; Duwe, M.; Abel, B.; Ropers, C. Nanostructure-enhanced atomic line emission. *Nature* **2012**, *485*, E1–E2.

[25] Sivis, M.; Duwe, M.; Abel, B.; Ropers, C. Extreme-ultraviolet light generation in plasmonic nanostructures. *Nat. Phys.* **2013**, *9*, 304–309.

[26] Pfullmann, N.; Waltermann, C.; Noack, M.; Rausch, S.; Nagy, T.; Reinhardt, C.; Kovačev, M.; Knittel, V.; Bratschitsch, R.; Akemeier, D. et al. Bow-tie nano-antenna assisted generation of extreme ultraviolet radiation. *New J. Phys.* **2013**, *15*, 093027.

[27] Kollmann, H.; Piao, X. J.; Esmann, M.; Becker, S. F.; Hou, D. C.; Huynh, C.; Kautschor, L. O.; Bösker, G.; Vieker, H.; Beyer, A. et al.

Toward plasmonics with nanometer precision: Nonlinear optics of helium-ion milled gold nanoantennas. *Nano Lett.* **2014**, *14*, 4778–4784.
[28] Kim, M. K.; Sim, H.; Yoon, S. J.; Gong, S. H.; Ahn, C. W.; Cho, Y. H.; Lee, Y. H. Squeezing photons into a point-like space. *Nano Lett.* **2015**, *15*, 4102–4107.
[29] Yoon, S. J.; Lee, J.; Han, S.; Kim, C. K.; Ahn, C. W.; Kim, M. K.; Lee, Y. H. Non-fluorescent nanoscopic monitoring of a single trapped nanoparticle via nonlinear point sources. *Nat. Commun.* **2018**, *9*, 2218.
[30] Wang, B.; Singh, S. C.; Lu, H. Y.; Guo, C. L. Design of aluminum bowtie nanoantenna array with geometrical control to tune LSPR from UV to Near-IR for optical sensing. *Plasmonics* **2020**, *15*, 609–621.
[31] Arshad, N. S.; Anwar, S.; Wahab, R.; Hussain, A.; Alam, M.; Ali, W.; Awan, T. I.; Nabi, G. Highly sensitive plasmonic au bowtie sensors with extraordinary optical absorbance for SERS applications. *Plasmonics*, in press, https://doi.org/10.1007/s11468-024-02388-0.
[32] Crozier, K. B.; Sundaramurthy, A.; Kino, G. S.; Quate, C. F. Optical antennas: Resonators for local field enhancement. *J. Appl. Phys.* **2003**, *94*, 4632–4642.
[33] Wang, Q. G.; Liu, L. J.; Wang, Y. F.; Liu, P.; Jiang, H. W.; Xu, Z.; Ma, Z.; Oren, S.; Chow, E. K. C.; Lu, M. et al. Tunable optical nanoantennas incorporating bowtie nanoantenna arrays with stimuli-responsive polymer. *Sci. Rep.* **2016**, *5*, 18567.
[34] Kaniber, M.; Schraml, K.; Regler, A.; Bartl, J.; Glashagen, G.; Flassig, F.; Wierzbowski, J.; Finley, J. J. Surface plasmon resonance spectroscopy of single bowtie nano-antennas using a differential reflectivity method. *Sci. Rep.* **2016**, *6*, 23203.
[35] Feng, L.; Ma, R. P.; Wang, Y. D.; Xu, D. R.; Xiao, D. Y.; Liu, L. X.; Lu, N. Silver-coated elevated bowtie nanoantenna arrays: Improving the near-field enhancement of gap cavities for highly active surface-enhanced Raman scattering. *Nano Res.* **2015**, *8*, 3715–3724.
[36] Laible, F.; Gollmer, D. A.; Dickreuter, S.; Kern, D. P.; Fleischer, M. Continuous reversible tuning of the gap size and plasmonic coupling of bow tie nanoantennas on flexible substrates. *Nanoscale* **2018**, *10*, 14915–14922.
[37] Pacheco-Peña, V.; Alves, R. A.; Navarro-Cía, M. From symmetric to asymmetric bowtie nanoantennas: Electrostatic conformal mapping perspective. *Nanophotonics* **2020**, *9*, 1177–1187.
[38] Hu, H.; Tao, W.; Laible, F.; Maurer, T.; Adam, P. M.; Horneber, A.; Fleischer, M. Spectral exploration of asymmetric bowtie nanoantennas. *Micro Nano Eng.* **2022**, *17*, 100166.
[39] Xiong, Y.; Hu, H. T.; Zhang, T. Z.; Xu, Y. H.; Gao, F.; Chen, W.; Zheng, G. C.; Zhang, S. P.; Xu, H. X. Quantitative and sensitive detection of alpha fetoprotein in serum by a plasmonic sensor. *Nanophotonics* **2022**, *11*, 4821–4829.
[40] Pei, H.; Peng, W. F.; Zhang, J. L.; Zhao, J. X.; Qi, J. L.; Yu, C. J.; Li, J.; Wei, Y. Surface-enhanced photoluminescence and Raman spectroscopy of single molecule confined in coupled Au bowtie nanoantenna. *Nanotechnology* **2024**, *35*, 155201.
[41] Li, S.; Tan, W. Y.; Liu, S. X.; Liu, G. Q.; Wang, Y.; Chen, J.; Tang, C. J.; Du, W.; Liu, Z. Q. Efficient photothermal therapy with spatially localized high-temperature generation by refractory absorber. *Appl. Phys. Lett.* **2023**, *123*, 131701.
[42] Yang, J. K. W.; Cord, B.; Duan, H. G.; Berggren, K. K.; Klingfus, J.; Nam, S. W.; Kim, K. B.; Rooks, M. J. Understanding of hydrogen silsesquioxane electron resist for sub-5-nm-half-pitch lithography. *J. Vac. Sci. Technol. B* **2009**, *27*, 2622–2627.
[43] Tisch, J. W. G.; Ditmire, T.; Fraser, D. J.; Hay, N.; Mason, M. B.; Springate, E.; Marangos, J. P.; Hutchinson, M. H. R. Investigation of high-harmonic generation from xenon atom clusters. *J. Phys. B: At. Mol. Opt. Phys.* **1997**, *30*, L709–L714.
[44] Vozzi, C.; Nisoli, M.; Caumes, J. P.; Sansone, G.; Stagira, S.; De Silvestri, S.; Vecchiocattivi, M.; Bassi, D.; Pascolini, M.; Poletto, L. et al. Cluster effects in high-order harmonics generated by ultrashort light pulses. *Appl. Phys. Lett.* **2005**, *86*, 111121.
[45] Park, H.; Wang, Z.; Xiong, H.; Schoun, S. B.; Xu, J. L.; Agostini, P.; DiMauro, L. F. Size-dependent high-order harmonic generation in rare-gas clusters. *Phys. Rev. Lett.* **2014**, *113*, 263401.
[46] Tao, Y.; Hagmeijer, R.; Bastiaens, H. M. J.; Goh, S. J.; van der Slot, P. J. M.; Biedron, S. G.; Milton, S. V.; Boller, K. J. Cluster size dependence of high-order harmonic generation. *New J. Phys.* **2017**, *19*, 083017.
[47] Johnson, P. B.; Christy, R. W. Optical constants of the noble metals. *Phys. Rev. B* **1972**, *6*, 4370–4379.
[48] Phillip, H. R.; Taft, E. A. Kramers-kronig analysis of reflectance data for diamond. *Phys. Rev.* **1964**, *136*, A1445–A1448.
[49] Malitson, I. H.; Dodge, M. J. Refractive index and birefringence of synthetic sapphire. *J. Opt. Soc. Am.* **1972**, *62*, 1405.
[50] Pan, L. S.; Kania, D. R. *Diamond: Electronic Properties and Applications*; Springer: New York, 1995.
[51] Cahill, D. G.; Lee, S. M.; Selinder, T. I. Thermal conductivity of κ-Al_2O_3 α-Al_2O_3 wear-resistant coatings. *J. Appl. Phys.* **1998**, *83*, 5783–5786.
[52] Chen, Q. J.; Song, C. W.; Zhang, H. J.; Huang, Y. D., Li, G.; Du, K. Study on the surface morphology formation mechanism of femtosecond laser processing gold. *Opt. Laser Technol.* **2024**, *169*, 110048.
[53] Kim, I.; Mun, J.; Hwang, W.; Yang, Y.; Rho, J. Capillary-force-induced collapse lithography for controlled plasmonic nanogap structures. *Microsyst. Nanoeng.* **2020**, *6*, 65.
[54] Kim, I.; Mun, J.; Baek, K. M.; Kim, M.; Hao, C. L.; Qiu, C. W.; Jung, Y. S.; Rho, J. Cascade domino lithography for extreme photon squeezing. *Mater. Today* **2020**, *39*, 89–97.
[55] Tiwari, N. R.; Liu, M. Y.; Kulkarni, S.; Fang, Y. Study of adsorption behavior of aminothiophenols on gold nanorods using surface-enhanced Raman spectroscopy. *J. Nanophotonics* **2011**, *5*, 053513.
[56] Hu, X. G.; Wang, T.; Wang, L.; Dong, S. J. Surface-enhanced Raman scattering of 4-aminothiophenol self-assembled monolayers in sandwich structure with nanoparticle shape dependence: Off-surface plasmon resonance condition. *J. Phys. Chem. C* **2007**, *111*, 6962–6969.
[57] Xiao, N.; Yu, C. X. Rapid-response and highly sensitive noncross-linking colorimetric nitrite sensor using 4-aminothiophenol modified gold nanorods. *Anal. Chem.* **2010**, *82*, 3659–3663.
[58] Zhang, W. Q.; Rahmani, M.; Niu, W. X.; Ravaine, S.; Hong, M. H.; Lu, X. M. Tuning interior nanogaps of double-shelled Au/Ag nanoboxes for surface-enhanced Raman scattering. *Sci. Rep.* **2014**, *5*, 8382.
[59] Liu, Y.; Chui, K. K.; Xia, X. Y.; Zhang, H.; Zhuo, X. L.; Wang, J. F. Selective deposition of a MOF at the spikes of Au nanostars for SERS detection. *Nano Res.*, in press, https://doi.org/10.1007/s12274-024-6737-8.
[60] May, P. W.; Smith, J. A.; Rosser, K. N. 785 nm Raman spectroscopy of CVD diamond films. *Diam. Relat. Mater.* **2008**, *17*, 199–203.
[61] Sallam, M. O.; Vandenbosch, G. A. E.; Gielen, G.; Soliman, E. A. Integral equations formulation of plasmonic transmission lines. *Opt. Express* **2014**, *22*, 22388–22402.
[62] Qayoom, T.; Najeeb-ud-din, H. Effective index approximation based analytical modeling and two dimensional numerical investigation of surface and bulk sensitivity in optimized hybrid nanostructured plasmonic gratings with miniaturized footprints. *Opt. Quant. Electron.* **2023**, *55*, 302.
[63] Kim, Y. S.; Moon, B.; Kim, C.; Ju, B. K.; Lee, J. H.; Jhon, Y. M. Optimizing high harmonic generation in hollow-core gas cell considering variation of gas density. *Opt. Laser Technol.* **2022**, *149*, 107803.

This is an open access article under the terms of the Creative Commons Attribution 4.0 International License (CC BY 4.0, https://creativecommons.org/licenses/by/4.0/).

© The Author(s) 2025. Published by Tsinghua University Press.